


---

This is the **submitted version** of the journal article:

Li, Junshan; Xu, Xijun; Yu, Xiaoting; [et al.]. «Monodisperse CoSn and NiSn nanoparticles supported on commercial carbon as anode for lithium- and potassium-ion batteries». ACS applied materials & interfaces, Vol. 12 issue 4 (Jan 2020), p. 4414-4422. DOI 10.1021/acsami.9b16418

---

This version is available at <https://ddd.uab.cat/record/235999>

under the terms of the  **IN** COPYRIGHT license

# Monodisperse CoSn and NiSn Nanoparticles Supported on Commercial Carbon as Anode for Lithium- and Potassium-ion Batteries

Junshan Li,<sup>Σ,π,○</sup> Xijun Xu,<sup>§,η,○</sup> Xiaoting Yu,<sup>Σ,π</sup> Xu Han,<sup>§</sup> Ting Zhang,<sup>ε</sup> Yong Zuo,<sup>Σ</sup> Chaoqi Zhang,<sup>Σ</sup> Dawei Yang,<sup>Σ</sup> Wang Xiang,<sup>Σ</sup> Zhishan Luo,<sup>Æ</sup> Jordi Arbiol,<sup>§,Δ</sup> Jordi Llorca,<sup>φ</sup> Jun Liu,<sup>§,η\*</sup> Andreu Cabot<sup>Σ,Δ\*</sup>

<sup>Σ</sup> Catalonia Institute for Energy Research - IREC, Sant Adrià de Besòs, Barcelona, 08930, Spain

<sup>π</sup> Departament d'Electrònica, Universitat de Barcelona, 08028 Barcelona, Spain

<sup>§</sup> Guangdong Provincial Key Laboratory of Advanced Energy Storage Materials, School of Materials Science and Engineering, South China University of Technology, Guangzhou 510641, P. R. China

<sup>η</sup> SUNWODA-SCUT Joint Laboratory for Advanced Energy Storage Technology, South China University of Technology, Guangzhou 510641, P. R. China

<sup>§</sup> Catalan Institute of Nanoscience and Nanotechnology (ICN2), CSIC and BIST, Campus UAB, Bellaterra, 08193 Barcelona, Spain

<sup>Æ</sup> Department of Chemistry, Southern University of Science and Technology (SUSTech), Shenzhen, Guangdong 518055, P. R. China

<sup>Δ</sup> ICREA, Pg. Lluís Companys 23, 08010 Barcelona, Spain

<sup>φ</sup> Institute of Energy Technologies, Department of Chemical Engineering and Barcelona Research Center in Multiscale Science and Engineering. Universitat Politècnica de Catalunya, EEBE, 08019 Barcelona, Spain

**KEYWORDS:** Colloidal nanoparticles; bimetallic alloys; anode; lithium-ion batteries; potassium-ion batteries.

**ABSTRACT:** Monodisperse CoSn and NiSn nanoparticles were prepared in solution and supported on commercial carbon black. The obtained nanocomposites were applied as anodes for Li- and K-ion batteries. CoSn@C delivered stable average capacities of 850, 650 and 500 mAh g<sup>-1</sup> at 0.2, 1.0 and 2.0 A g<sup>-1</sup>, respectively, well above those of commercial graphite anodes. The capacity of NiSn@C retained up to 575 mAh g<sup>-1</sup> at a current of 1.0 A g<sup>-1</sup> over 200 continuous cycles. Up to 74.5% and 69.7% pseudocapacitance contribution for Li-ion batteries were measured for CoSn@C and NiSn@C, respectively, at 1.0 mV s<sup>-1</sup>. CoSn@C was further tested in full-cell lithium ion batteries with a LiFePO<sub>4</sub> cathode to yield a stable capacity of 350 mAh g<sup>-1</sup> at a rate of 0.2 A g<sup>-1</sup>. As electrode in K-ion batteries, CoSn@C composites presented a stable capacity of around 200 mAh g<sup>-1</sup> at 0.2 A g<sup>-1</sup> over 400 continuous cycles, and NiSn@C delivered a lower capacity of around 100 mAh g<sup>-1</sup> over 300 cycles.

## INTRODUCTION

With an ever increasing demand for portable electronics, the market for rechargeable lithium-ion batteries (LIBs) have exponentially grown since their first commercialization in 1991.<sup>1,2</sup> However, current LIBs still do not meet the desired targets on safety, durability and energy density.<sup>3</sup> Centering on the anode, commercial LIBs currently use graphite, which presents moderate theoretical capacities, 372 mAh g<sup>-1</sup>,<sup>4</sup> leaving plenty of room for improvement. Beyond graphite, Sn, Sb, Si and Ge can alloy with Li to provide much higher energy densities.<sup>5-10</sup> Among them, Sn and its alloys are especially

interesting due to their abundance, low cost and large electrical conductivity.

A critical challenge for these anode materials and particularly Sn is a poor cycling performance associated with a large volume variation upon lithium ion insertion/extraction.<sup>11-14</sup> To buffer these volume changes, several stratagems have been developed, including the nanostructuring of the electroactive elements, its alloying with additional metals, its encapsulation within a shell, and its combination with carbon-based materials.<sup>15-26</sup>

On the other hand, the limited availability of lithium and the related high price of this element may soon constrain the LIBs market growth, especially in

applications requiring large-scale storage. Thus, rechargeable batteries based on more abundant and low-cost raw materials are highly desirable. In this direction, sodium-ion batteries (SIBs) and potassium-ion batteries (KIBs) are gathering increasing interest owing to the high abundance of Na and K.<sup>26–31</sup>

Recently we reported a series of monodisperse  $\text{Ni}_x\text{Sn}$  and  $\text{Co}_x\text{Sn}$  nanoparticles (NPs) as anodes for LIBs and SIBs.<sup>29,30</sup> We found the best stoichiometry to be close to  $x=1$ . In this work, we report a significant increase of stability of these anodes by proper ligand removal and by supporting the NPs on carbon black. The material performance is analyzed not only in half-cell electrochemical experiments, but also in full-cell LIBs with  $\text{LiFePO}_4$  as cathode. Additionally, we study here the electrochemical performance of  $\text{CoSn}$  and  $\text{NiSn}$  as anode material in KIBs.

## EXPERIMENTAL

**Chemicals:** Cobalt(II) acetylacetonate ( $\text{Co}(\text{acac})_2$ , 99%, Sigma-Aldrich), nickel(II) acetylacetonate ( $\text{Ni}(\text{acac})_2 \cdot x\text{H}_2\text{O}$  ( $x \sim 2$ ), 95%, Sigma-Aldrich), tin(II) acetate ( $\text{Sn}(\text{oac})_2$ , 95%, Fluka), oleic acid (OAc, Sigma-Aldrich), oleylamine (OAm, 80–90%, TCI), borane tert-butylamine complex (TBAB, 97%, Sigma-Aldrich), tri-*n*-octylphosphine (TOP, 97%, Strem), urea ( $\text{C}_7\text{H}_7\text{BrN}_2\text{O}$ , >98.0%, Aladdin), potassium stannate trihydrate ( $\text{K}_2\text{SnO}_3 \cdot 3\text{H}_2\text{O}$ , 95%, Aladdin), glucose ( $\text{C}_6\text{H}_{12}\text{O}_6$ , 99.5%, Aladdin), acetonitrile ( $\text{CH}_3\text{CN}$ , extra dry, Fisher), carbon black (CB, Vulcan XC72), hydrazine monohydrate ( $\text{N}_2\text{H}_4$ , 64–65%, reagent grade, 98%, Sigma-Aldrich), Carbon Super P (Super P, KJ group), *N*-methyl-2-pyrrolidone (NMP, 99%, Aladdin), polyvinylidene fluoride (PVDF, KJ group), ethylene carbonate (EC), fluoroethylene carbonate (FEC), diethyl carbonate (DEC), potassium bis-trifluoromethanesulfonylimide (KTFSI), and diglyme (DME) were used without further purification. Analytical-grade acetone, chloroform and ethanol were purchased from different supplier. A small glove-box filled with Ar was used for the manipulation and storage of sensitive chemicals.

**Synthesis of  $\text{CoSn}$  and  $\text{NiSn}$  NPs:** Syntheses of monodisperse NPs were conducted in a three-necked flask with a thermocouple, condenser, and septum. In a typical synthesis of  $\text{CoSn}$  NPs, 0.6 mmol  $\text{Sn}(\text{oac})_2$ , 0.9 mmol  $\text{Co}(\text{acac})_2$ , 20 mL of OAm and 1.0 mL of OAc were loaded into a 50 mL flask with a magnetic bar. Subsequently, the flask was kept at 80 °C under vacuum for 2 hours to remove water and other organics. Then, the flask was protected with a gentle flow of Ar, 5 mL TOP were injected, and subsequently the temperature was ramped at 5 °C  $\text{min}^{-1}$  to 180 °C. In the meantime, 5 mmol of TBAB was sonicated in 5 mL OAm for 0.5 hours and then degassed with Ar for 1 hour. Upon injection of this reductant to the flask containing the Co and Sn precursors at 180 °C, the solution immediately turned black. The flask was maintained for 1 hour at this temperature to enable the NPs to grow. Then we removed

the heating mantle and the flask was shortly cooled to ambient temperature in a water bath.  $\text{NiSn}$  NPs were synthesized using the same procedure, but replacing  $\text{Co}(\text{acac})_2$  by  $\text{Ni}(\text{acac})_2$ . NPs were centrifuged at a high speed after adding a proper amount of acetone. Then, chloroform was used to disperse the precipitate. A small portion of solution was dropt on a Cu mesh for electron microscopy analyses. Then the NPs were collected again with the help of acetone and they were repeatedly washed with acetone and chloroform.

**$\text{CoSn}$  and  $\text{NiSn}$  NP-carbon nanocomposites:** Before supporting the NPs on carbon black, surface ligands were removed using a mixture of diluted hydrazine hydrate in acetonitrile, following a previously reported protocol (see details in the SI).<sup>32</sup> Ligand-free NPs were subsequently supported on commercial CB as follows: First, 100 mg dried NPs and 30 mg CB together with 25 mL ethanol were mixed into a 50 mL vial. Afterward the mixture was vigorously sonicated for 1 hour at ambient temperature. Then, the material was centrifuged and dried in vacuum for over 2 nights. The product was kept in the glove box until further use. The terminology  $\text{CoSn}@C$  and  $\text{NiSn}@C$  was used to label these two nanocomposites.

**$\text{Sn}@C$  nanocomposites:**  $\text{SnO}_2$  hollow nanospheres were fabricated by a one-pot hydrothermal treatment, according to our previous work.<sup>33</sup> Simply, 0.48 g urea and 0.384 g  $\text{K}_2\text{SnO}_3 \cdot 3\text{H}_2\text{O}$  were dissolved in a mixture of ethanol and distilled water. Then this mixture was located into an autoclave containing a Teflon liner that was heated at 190 °C for 15 h. The product of the hydrothermal reaction was collected, washed with ethanol and distilled water, and then dried under vacuum. To obtain  $\text{Sn}@C$ , 0.17 g of as-prepared  $\text{SnO}_2$  hollow nanospheres and 0.68 g glucose were treated in a sealed autoclave at 190 °C for a period of 10 h and subsequently annealed at 650 °C in an  $\text{H}_2/\text{Ar}$  flow for 6 h to reduce the  $\text{SnO}_2$  to Sn.

**Characterization:** The structure of the NPs and nanocomposites was analyzed by means of X-ray diffraction (XRD) on a Bruker AXS D8 Advance X-ray diffractometer with Cu K radiation. NPs size and morphology were observed by transmission electron microscopy (TEM) on a Zeiss Libra 120. Scanning TEM (STEM) and high-resolution TEM (HRTEM) were performed on a FEI Tecnai F20 microscope. Electron energy loss spectroscopy (EELS) and high angle annular dark-field (HAADF) STEM were carried out using a Gatan Quantum filter. Energy dispersive X-ray spectroscopy (EDS) analysis was carried out at 20 kV within a ZEISS Auriga scanning electron microscope (SEM). Compositions were obtained by averaging results from at least 3 points. X-ray photoelectron spectroscopy (XPS) spectra were obtained with a SPECS system in normal emission. The presence of surface ligands was determined using a Alpha Bruker Fourier transform infrared spectrometer (FTIR). The materials' pore size distribution and specific surface area were analyzed by means of  $\text{N}_2$  adsorption using a Tristar II 3020 Micromeritics system. Specific surface areas were determined by means of the Brunauer–Emmet–Teller (BET) approach, considering

equally spaced points in the P/Po range. The pore size distribution was calculated from the isotherms desorption branches using the Barrett-Joyner-Halenda (BJH) approach.

**Electrochemical measurements:** The performance of NP-based electrodes was analyzed using a battery test system (CT2001A, LAND). Half cells were fabricated in an argon-filled glove box with  $\text{H}_2\text{O}$  and  $\text{O}_2$  level lower than 0.1 ppm using Celgard2400 as separator. The ink was obtained by mixing NPs, PVDF and Super P (80:10:10 in weight ratio) with NMP. Then, to prepare the working electrode, the mixture was coated on Cu and it was subsequently dried in vacuum at 80 °C during 24 h. Then, disks with a diameter of 12 mm were cut from the foil. The electrolyte for LIBs was composed of a 1 M  $\text{LiPF}_6$  solution in EC/DEC (1:1 in volume) with 5 wt% FEC as additive. For electrochemical measurements, cyclic voltammetry (CV) was conducted on an electrochemical workstation (Gamry Interface 1000) in the potential window 0.01–3.0 V using scan rates in the range 0.1–1  $\text{mV s}^{-1}$ . Electrochemical impedance spectroscopy (EIS) measurements were performed using a 5 mV modulation amplitude in a frequency range 0.1–10<sup>6</sup> Hz. For the lithium-ion full-cell,  $\text{LiFePO}_4$  on Al foil (MTI Corporation, 10.95  $\text{mg cm}^{-2}$ ) was used as cathode materials. The anodic capacities were normalized to the mass of the whole materials in both half- and full-cell experiments. For potassium ion half-cell, 3 M KTFSI in DME was used as electrolyte, Whatman GF/D as the separator and K flakes as counter electrodes.

## RESULTS AND DISCUSSION

Colloidal CoSn ( $6 \pm 0.8$  nm) and NiSn NPs ( $4.2 \pm 0.7$  nm) were produced in solution from the reduction of proper precursors in a solution containing OAm, OAc and TOP (see the experimental details, Figures 1a and S1).<sup>29,30</sup> After purifying the NPs by multiple precipitation and re-dispersion steps, surface organic ligands were removed, as confirmed by FTIR spectroscopy (Figure S2). Subsequently, Sn-based NPs and carbon black were physically mixed in solution by sonication for 1 hour. A uniform distribution of the two phases within the CoSn@C and NiSn@C nanocomposites was evidenced by SEM-EDS elemental maps (Figures S3 and S4). According to EDS analysis, atomic ratios for CoSn and NiSn NPs were Co/Sn~1 and Ni/Sn~1, respectively (Figure S5). Figure S6a shows the type IV adsorption-desorption isotherms obtained from the as-prepared nanocomposites and carbon black. High BET specific surface areas of 51.5  $\text{m}^2 \text{g}^{-1}$  and 56.2  $\text{m}^2 \text{g}^{-1}$ , were calculated for NiSn@C and CoSn@C. As displayed in Figure S6b, BJH plots revealed the composites to be characterized by broad pore size distribution in the mesoporous and microporous range, similar to carbon black.

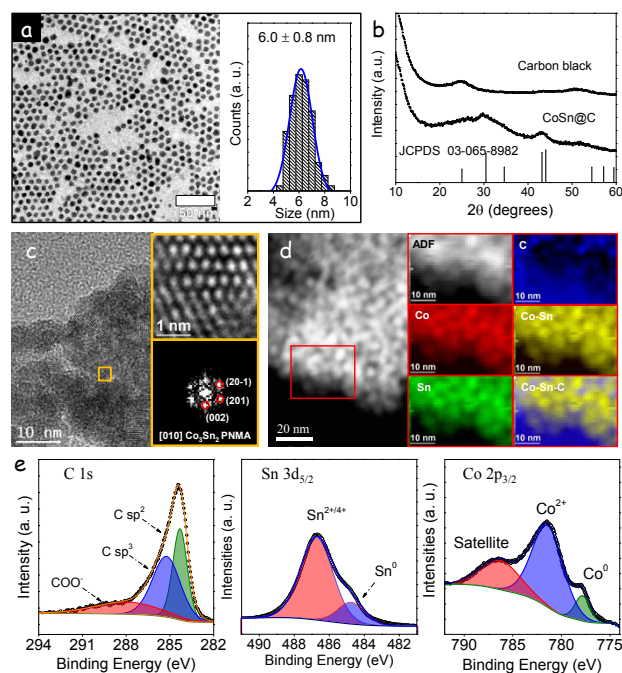


**Figure 1.** a) Representative TEM micrograph of CoSn NPs and their size distribution histogram. b) XRD patterns of CoSn NPs and a CoSn@C composite. c) HRTEM micrograph of a CoSn@C composite and detail of the yellow square with its corresponding power spectrum. d) STEM-HAADF micrograph and EELS elemental maps of a CoSn@C composite showing individual Co  $L_{2,3}$ -edges at 779 eV (red), Sn M-edge at 485 eV (green) and C K-edge at 284 eV (blue) as well as their composites: Co-Sn and Co-Sn-C. e) XPS spectra of the C 1s, Sn  $3d_{5/2}$  and Co  $2p_{3/2}$  regions of the CoSn@C composite.

XRD patterns of the carbon black and a CoSn@C composite are displayed in Figure 1b. The broad peak at 25° was ascribed to the (002) crystallographic plane of carbon. The two peaks at around 31° and 44° observed in the nanocomposite XRD pattern matched with the  $\text{Co}_3\text{Sn}_2$  phase.<sup>34</sup> HRTEM micrographs and power spectra analyses confirmed the crystallographic phase of CoSn alloy NPs to match with the  $\text{Co}_3\text{Sn}_2$  orthorhombic phase in PNMA space group. From the crystalline domain in Figure 1c, the  $\text{Co}_3\text{Sn}_2$  lattice fringe distances were 0.328 nm, 0.403 nm, and 0.330 nm, at 63.46° and 47.61° which were assigned to the  $\text{Co}_3\text{Sn}_2$  orthorhombic phase, visualized along the [010] zone axis. The unit cell parameters were  $a = 7.1450$ ,  $b = 5.2500$  Å and  $c = 8.1730$  Å (Figure 1d). EELS elemental composition maps revealed a uniform distribution of Co and Sn (Figure 1d). Besides, XRD and HRTEM analyses evidenced the structure of NiSn NPs to match the  $\text{Ni}_3\text{Sn}_2$  orthorhombic phase, consistently with our previous report (Figure S7).<sup>29</sup>

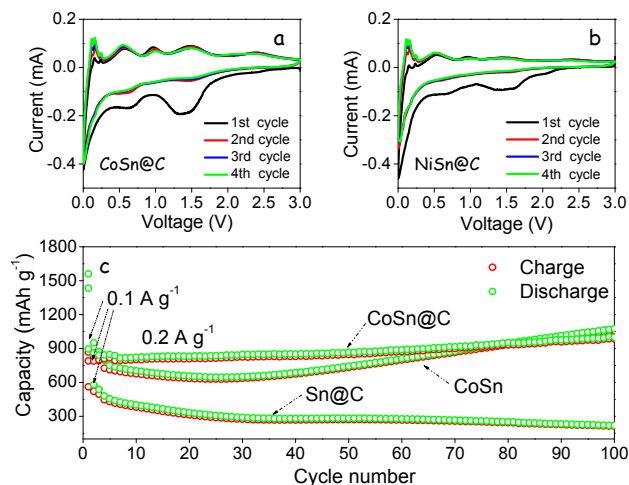


**Figure 2.** Initial cyclic voltammograms obtained in the voltage window 0–3.0 V vs. Li<sup>+</sup>/Li at 0.1 mV s<sup>-1</sup> from nanocomposite electrode: a) CoSn@C, b) NiSn@C. c) Charge-discharge capacity and the related coulombic efficiency over 100 cycles at a current density of 0.2 A g<sup>-1</sup> for CoSn@C, bare CoSn and Sn@C electrodes: activated at 0.1 A g<sup>-1</sup> for 10 cycles each.

The XPS spectra of CoSn@C are shown in Figures 1e and S8. The C 1s region was fitted with three peaks at 284.3 eV, 285.3 eV and 288.1 eV, matching C sp<sup>3</sup>, sp<sup>2</sup> and COO<sup>-</sup> respectively. Two tin chemical states were identified, at 484.7 eV (Sn 3d<sub>5/2</sub>) and 486.7 eV (Sn 3d<sub>3/2</sub>), assigned to a metallic Sn<sup>0</sup> environment and a Sn<sup>2+</sup> or Sn<sup>4+</sup> oxidized state, respectively. Co was present in two different chemical states, metallic Co<sup>0</sup> at 777.8 eV (Co 2p<sub>3/2</sub>) and Co<sup>2+</sup> at 781.5 eV (Co 2p<sub>3/2</sub>). The surface oxidation was consistent with the exposure of the NPs to ambient atmosphere during purification, ligand removal and handling.<sup>35–38</sup> The surface atomic ratio of CoSn NPs measured by XPS was Sn/Co=2.6. This result indicated that the NPs surface was Sn rich, which could be associated with a preferential diffusion of Sn toward the surface during oxidation.<sup>30,39</sup>

Initial electrochemical tests were performed in Li-ion half-cells with elemental lithium as counter and reference electrode. Electrodes were printed from slurries containing 80 wt% of nanocomposites as active material, 10 wt% PVDF as binder and 10 wt% Super P as conductive additive. Figure 2ab display CV curves for CoSn@C and NiSn@C obtained at 0.1 mV s<sup>-1</sup> in the applied potential range 0–3.0 V vs. Li/Li<sup>+</sup>. Both electrodes displayed similar CV curves. During the first charging process, a broad peak at 1.2–2.0 V was clearly displayed, but disappear in the following few circles. This peak was attributed to the growth of the solid-electrolyte interface (SEI) layer and the irreversible lithiation of the surface oxidized layer formed during NP washing, handling and ligand-removing processes.<sup>40,41</sup> The well-overlapped 2<sup>nd</sup>–4<sup>th</sup> CV curves indicated a good cycling performance of CoSn@C and NiSn@C anode.

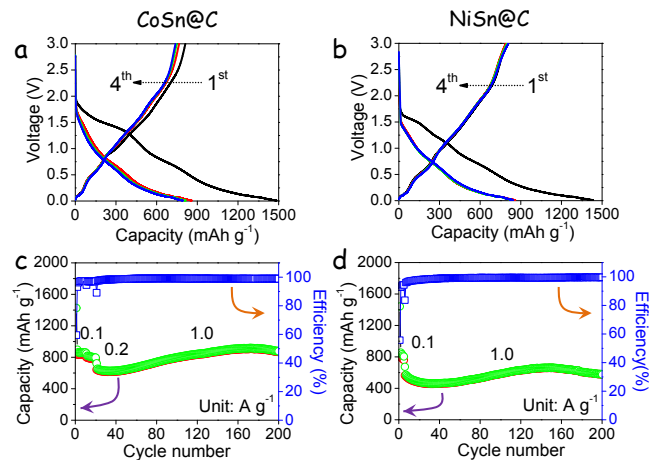


**Figure 3.** a-b) Initial 4 CV curves at 0.1 A g<sup>-1</sup> for CoSn@C and NiSn@C electrodes. c-d) Charge-discharge capacity and its coulombic efficiency over 200 cycles at 1.0 A g<sup>-1</sup>: activated at 0.1 A g<sup>-1</sup> for 10 cycles each. For the CoSn@C electrode, additional 10 activation cycles were conducted at 0.2 A g<sup>-1</sup>.

Figure 2c compares the cycling performance of CoSn@C, unsupported CoSn and Sn@C electrodes at 0.2 A g<sup>-1</sup>. For the CoSn-based electrode, the stability and capacity were significantly enhanced with the presence of carbon. Note that the capacity values plotted in this figure are referred to the whole mass of material coated on the Cu support, i.e. it takes into account both the mass of NPs and carbon in the case of CoSn@C composites. If capacities were referred to the amount of NPs, differences between CoSn@C and unsupported CoSn would be much more evident. In other words, properly supporting the NPs on carbon black allowed replacing part of the active material with carbon while maintaining similar overall capacities. The enhanced cycling performance of CoSn@C compared with bare CoSn was ascribed to the accommodation of structural strain of CoSn within the carbon matrix, the improved electrical conductivity of the composite, the high NP dispersion and the shorter charge transportation lengths for Li ions due to the higher electrode porosity.<sup>42</sup>

Besides, when compared with Sn@C, CoSn@C delivered a twofold increase of the average capacity, up to 800 mAh g<sup>-1</sup> over 100 continuous cycles. The higher capacities experimentally obtained in the present work for alloy NPs compared when with bare Sn may be partially related to the smaller size of the alloy NPs and the different synthesis protocols used (Figure S9). However, taking into account previous literature on Sn-based LIBs, we associated the improved capacity of our alloys with respect to Sn@C to a size change buffering effect associated to the presence of Co,<sup>43</sup> and a very large pseudocapacitive contribution in the alloy electrodes, as discussed below.

As shown in Figures 3a and 3c, at a higher charge-discharge rate, 1.0 A g<sup>-1</sup>, the initial coulombic efficiency for CoSn@C electrodes was 59.5% with high reversible capacities (848.4 mA g<sup>-1</sup>) and discharge capacities (1426



mA g<sup>-1</sup>). For the following 10 cycles at 0.1 A g<sup>-1</sup>, the capacity decreased, which was associated with the SEI formation and an irreversible Li<sup>+</sup> insertion in the surface oxide layer. After additional 10 cycles at 0.2 A g<sup>-1</sup>, the capacity was relatively stable at around 700 mAh g<sup>-1</sup> for over 180 cycles at 1.0 A g<sup>-1</sup> with a coulombic efficiency up to 100%. Actually, a slight increase of capacity was obtained with the cycle number above 40 cycles. This increase of capacity is a common observation in Sn-based transition metal alloys and is assigned to several factors, including restructuration of the material, creation of additional paths for electrolyte diffusion, increase of pseudocapacitive contribution, and increased rate of lithiation/delithiation of the material.<sup>43–45</sup>

When comparing the electrochemical performance of LIBs at the same charging-discharging rate, the capacity for NiSn@C was lower than that of CoSn@C electrode, which is in good agreement with our earlier report.<sup>29,30</sup> NiSn@C electrodes provided an average capacity of 500 mAh g<sup>-1</sup> (Figures 3b and 3d) at 1.0 A g<sup>-1</sup> and 400 mAh g<sup>-1</sup> over 200 cycles at 2.0 A g<sup>-1</sup> (Figure S10). The origin of the higher performance of CoSn- with respect to NiSn-based electrodes is not clear at this point, but it may be related to the higher pseudocapacitance provided by the former or to a higher rate of oxidation of the smaller NiSn NPs compared with CoSn.

Overall, Sn-based NPs@C nanocomposites provided enhanced performance when compared with graphite and most previous Sn-based alloys (Table S1). We associated the superior electrochemical performance of our anodes to the very small size of the alloy domains, their excellent dispersion over the carbon support and the large surface area and porous character of the overall composite, which provided a high electrode-electrolyte interface and a large density of Li-ion diffusion avenues through an electrically highly conductive and mechanically stable support.

To evaluate the rate capability, galvanostatic cycling was conducted at various current rates ranging from 0.1 to 5 A g<sup>-1</sup>. As displayed in Figures 4a and 4b, CoSn@C electrodes delivered a discharge capacity of 882.3, 846.2, 735.1, 640.8, 526.8, 298.2 mA g<sup>-1</sup> at 0.1, 0.2, 0.5, 1.0, 2.0 and 5.0 A g<sup>-1</sup>, respectively. NiSn@C delivered lower rate capability, with 798.6, 668, 497.9, 376.3, 279.3, 162.6 mA g<sup>-1</sup> at the same testing rates (Figure S11). Additionally, the CoSn@C anode delivered a stable capacity at 0.1, 0.2, 0.5 and 1.0 A g<sup>-1</sup> after 60 cycles at variable charging rates. We associated the excellent cycling performance and rate capability of CoSn@C to the nanometric size of the electroactive material, its proper composition and its combination with a high surface area and porous carbon matrix that prevented NP aggregation and disconnection, and facilitated Li<sup>+</sup> diffusion and charge transport.

We further investigated the electrode kinetics using EIS. The Nyquist plots measured from CoSn@C and NiSn@C and the equivalent circuits are displayed in Figure S12 and the fitted values are summarized in Table S2. At high frequencies, the diffusion resistance of CoSn@C was observed to be slightly larger than that of

NiSn@C, but with a smaller charge-transfer resistance. The inclined line in the low frequency part of the Nyquist plots, reflecting the kinetics of the Li<sup>+</sup> uptake/release,<sup>46</sup> was linearly fitted with the square root of angular frequency ( $\omega$ ), see Figure S13.<sup>47</sup> From this fitting, the lithium ion diffusion coefficient for LIBs was calculated to be  $9.25 \times 10^{-15}$  cm<sup>2</sup> s<sup>-1</sup> for CoSn@C and  $2.34 \times 10^{-15}$  cm<sup>2</sup> s<sup>-1</sup> for NiSn@C (see details in the SI). Surprisingly, the ohmic resistance and charge-transfer resistance between the anode and the electrolyte obtained from the semicircle in the medium-frequency range was significantly larger for CoSn@C than for NiSn@C (Table S2).

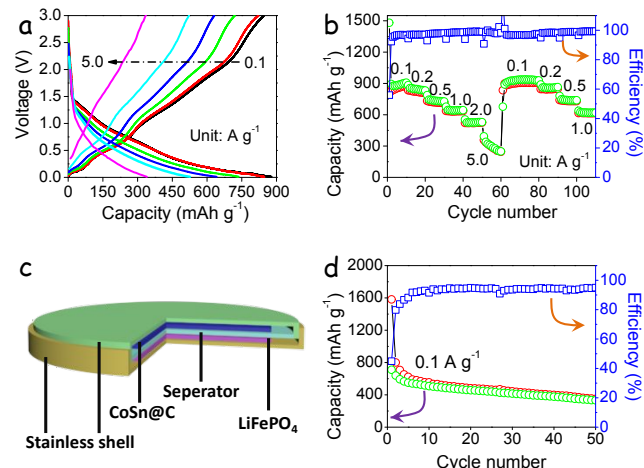


**Figure 4.** Li-ion storage performance of the CoSn@C composite electrode: a) Charge-discharge CV curves at rates: 0.1, 0.2, 0.5, 1.0, 2.0, 5.0 A g<sup>-1</sup>. b) The corresponding rate performance. c) Schematic drawing of the full-cell set up. d) Galvanostatic charge-discharge curves of a lithium-ion full-cell battery with CoSn@C as anode and LiFePO<sub>4</sub> as cathode materials.

To further investigate the applicability of CoSn@C composites as anode in LIBs, full cells were assembled and tested using LiFePO<sub>4</sub> as cathode material (Figure 4c). CoSn@C//LiFePO<sub>4</sub> cells were cycled galvanostatically at a current density of 0.1 A g<sup>-1</sup> in the potential window 0.5–3.2 V. As shown in Figure 4d, a fast loss in the capacity was obtained with the formation of the SEI layer within the initial 10 cycles at 0.1 A g<sup>-1</sup>. Afterward, the capacity was stabilized at 350 mAh g<sup>-1</sup> with around 95% coulombic efficiency over the following 40 cycles.

The capacitive contribution of CoSn@C anodes was further studied using CV measurements. Figure 5a presents the CV curves at various scan rates 0.1–1.0 mV s<sup>-1</sup> in the potential range 0–3.0 V vs. Li<sup>+</sup>/Li. Two obvious anodic peaks were identified at around 0.57 and 1.49 V, with a peak current that increased with the scan rate. Generally, the measured current ( $i$ ) is considered as a function of scan rate ( $v$ ) as follows:

$$i = av^b$$

where  $a$  and  $b$  are empirical values.<sup>48–51</sup> In previous reports, a diffusion-controlled process was characterized by  $b = 0.5$ , whereas  $b = 1$  was associated with an ideal capacitive behavior. From our measurements, the  $b$  value

at the two peaks was calculated to be 0.68 and 0.85 respectively (Figure 5b), which was consistent with a fast kinetics arising from an important pseudocapacitive effect.

We further divided the capacity contribution at each scan rate and potential into the diffusion-controlled ( $k_1 v^{1/2}$ ) and the capacitance contribution ( $k_2 v$ ) using the following equation:<sup>52–55</sup>

$$i(V) = k_1 v^{1/2} + k_2 v$$

which can be rewritten as:

$$i(V)/v^{1/2} = k_1 + k_2 v^{1/2}$$

$k_1$  and  $k_2$  were determined from the dependence of  $i(V)/v^{1/2}$  vs.  $v^{1/2}$ . Figure 5c shows the CV profiles at 1.0  $\text{mV s}^{-1}$  where the capacitive current (in red filling) is differentiated from the total current (blue line). Similarly, contributions of the capacitive part at 0.1, 0.2, 0.4, 0.6 and 0.8  $\text{mV s}^{-1}$  are presented in Figure S13, and summarized in Figure 5d for comparison. When increasing sweep rates from 0.1 to 1.0  $\text{mV s}^{-1}$ , the capacitive contribution increased from 45.8% to 74.5%. These capacitive values are lower than those measured for bare CoSn NPs under the same scanning rates.<sup>30</sup> A similar trend was observed for NiSn@C composites, with a capacity contribution increase from 39.0% to 69.7%, slightly lower than those of CoSn@C (Figure S14). These results are in good agreement with the superior rate performance of CoSn@C when compared with NiSn@C electrodes. Besides, the above analysis evidenced that pseudocapacitance had a dominant role in the measured electrode capacity.

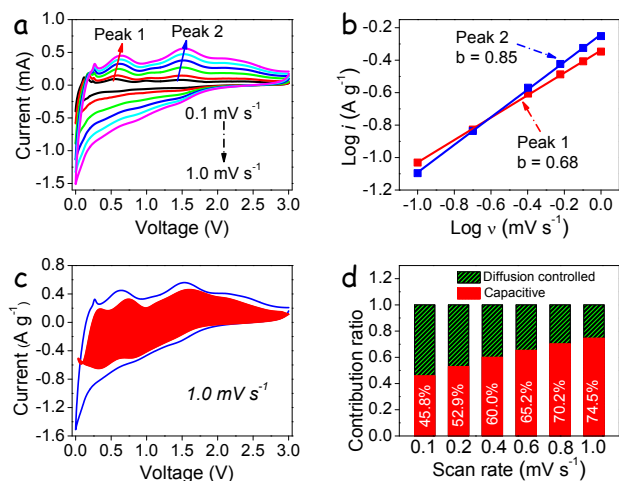


**Figure 5.** Kinetic analysis of CoSn@C as Li-ion anode: a) CV curves with scan rates from 0.1 to 1.0  $\text{mV s}^{-1}$ . b) CV peak current as a function of the sweep rate. c) Capacitive (shaded region) and diffusion current contributions at 1.0  $\text{mV s}^{-1}$ . d) Normalized capacitive- and diffusion-controlled contribution at different scan rate.

Based on the detailed electrochemistry and structural analysis, the superior performance of CoSn@C electrodes in LIBs could be associated with its hierarchical structure. The well-defined CoSn NPs with carbon supports could buffer the volume expansion to maintain the structural integrity of CoSn@C anode upon cycling.

Beyond  $\text{Li}^+$ ,  $\text{K}^+$  can be also reversibly stored and released from Sn-based anode materials, although with a relatively lower theoretical capacity of  $226 \text{ mAh g}^{-1}$ .<sup>56</sup> Despite its lower maximum capacity, the use of K finds advantages in terms of resource availability and cost, which are two main drawbacks of LIBs in a large scale energy storage scenario.

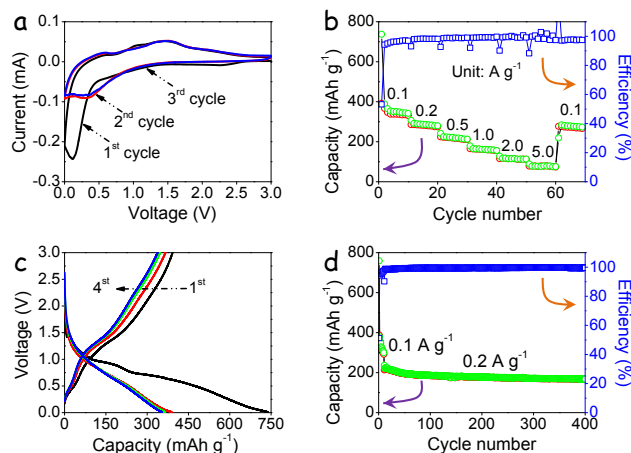


**Figure 6.** Potassium-ion storage performance of the CoSn@C electrode: a) Initial CV curves obtained in the voltage window 0–3.0 V vs.  $\text{K}^+/\text{K}$  at 0.1  $\text{mV s}^{-1}$ . b) Rate performance at 0.1, 0.2, 0.5, 1.0, 2.0, 5.0  $\text{A}$  and 0.1  $\text{A g}^{-1}$ . c) Initial charge-discharge curves at 0.1  $\text{A g}^{-1}$ . d) Charge-discharge capacity and its coulombic efficiency over 400 cycles at 0.2  $\text{A g}^{-1}$ : activated at 0.1  $\text{A g}^{-1}$  for 10 cycles.

KIB half cells were assembled in the same way as LIBs, except for the use of 3 M KTFSl in DME as  $\text{K}^+$  electrolyte. Figure 6a shows CV profiles of a CoSn@C composite measured at 0.1  $\text{mV s}^{-1}$  in the applied potential range of 0–3.0 V vs.  $\text{K}^+/\text{K}$ . The significant differences obtained between the initial and the following cycles were associated to the formation of SEI and the irreversible K insertion in the oxide layer. The rate capability of the CoSn@C composite was analyzed in the range between 0.1 to 5  $\text{A g}^{-1}$ . As can be seen in Figure 6b, the CoSn@C electrode delivered a discharge capacity of 351, 286.9, 221.5, 161.8, 115.2 and 76.7  $\text{mAh g}^{-1}$  at 0.1, 0.2, 0.5, 1.0, 2.0 and 5.0  $\text{A g}^{-1}$ , respectively. As shown in Figure S15ab, NiSn@C delivered lower capacities, with 322.4, 259.8, 184.3, 125.6, 73.8 and 44.8  $\text{mAh g}^{-1}$  at the same testing rate. The slightly higher capacitances obtained for CoSn are in consistency with results obtained for LIBs and may also find its origin on a higher relative oxidation of NiSn and a larger pseudocapacitance associated to Co.

The cycling performance of these two composites was obtained by galvanostatic charging-discharging at a high current density of 0.2  $\text{A g}^{-1}$  (Figure 6cd). CoSn@C electrodes delivered very large initial capacities, but displayed an obvious capacity loss during the first few cycles associated with the formation of the SEI layer. After additional 390 cycles, the capacities were stabilized at around 200  $\text{mAh g}^{-1}$  with high coulombic efficiency. As in LIBs, the NiSn@C composite presented lower electrochemical performance towards KIBs as displayed in

Figure S15cd. A comparison of our results with those obtained for other Sn-related materials as KIB anode materials is provided in Table S3.

EIS spectra obtained in KIBs was similar to that obtained in LIBs (Figure S16a). However, larger resistance values were obtained in KIBs than in LIBs when using the same fitting circuit (Table S4, Figure S16b). Besides, the  $K^+$  diffusion coefficient for CoSn@C and NiSn@C was  $1.38 \times 10^{-14} \text{ cm}^2 \text{ s}^{-1}$  and  $1.08 \times 10^{-14} \text{ cm}^2 \text{ s}^{-1}$ , higher than those obtained for  $\text{Li}^+$  diffusion. Overall, EIS result were consistent with the larger radius of  $K^+$  than  $\text{Li}^+$  and the fact that each Sn is able to accommodate 1  $K^+$  and 4.4  $\text{Li}^+$ .

## Conclusions

In conclusion, monodisperse CoSn and NiSn NPs were synthesized via a facile solution-based approach. After removing the surface ligands, NPs were supported on commercial carbon materials. The obtained nanocomposites were tested as anode materials in half-cell LIBs and KIBs and full-cell LIBs. CoSn@C electrodes displayed an excellent performance, with LIB half-cell charge-discharge capacities over more than one hundred cycles above 850, 650 and 500  $\text{mAh g}^{-1}$  at current densities of 0.2, 1.0 and 2.0  $\text{A g}^{-1}$ , respectively. These values were significantly larger than the theoretical maximum of graphite. As for LIB full-cells, CoSn@C electrodes delivered average capacities of 400  $\text{mAh g}^{-1}$  at a rate of 0.1  $\text{A g}^{-1}$ . Through the kinetic analysis of CoSn@C and NiSn@C nanocomposite by CV, it was found that charge-discharge capacities included very large pseudocapacitive contributions up to 74.5% at 1  $\text{mV s}^{-1}$  for CoSn@C and 69.7% for NiSn@C. These materials were also tested as anodes in KIBs. KIB capacities were stabilized at around 200  $\text{mAh g}^{-1}$  with high coulombic efficiency over 400 cycles for CoSn@C and 100  $\text{mAh g}^{-1}$  for NiSn@C over 300 cycles.

## Conflicts of interest

There are no conflicts to declare.

## ASSOCIATED CONTENT

**Supporting Information.** This material is available free of charge via the Internet at <http://pubs.acs.org>. For instance, additional TEM, XRD, ligand removal, FT-IR, SEM-EDS, XPS and additional electrochemical performance in LIBs and KIBs are presented.

## AUTHOR INFORMATION

Corresponding Author

\* Andreu Cabot: [acabot@irec.cat](mailto:acabot@irec.cat)

\* Jun Liu: [msjliu@scut.edu.cn](mailto:msjliu@scut.edu.cn)

Author Contributions

○ J. Li and X. Xu equally contributed to this work.

## ACKNOWLEDGMENT

This work was funded by the European Regional Development Funds and by the Spanish Ministerio de Economía y Competitividad within the project SEHTOP

(ENE2016-77798-C4-3-R). J. Li is grateful for the China Scholarship Council (CSC) support. This project was also supported by the National Natural Science Foundation of China (no. 51771076), the “1000 plan”, and the Project of Public Interest Research and Capacity Building of Guangdong Province (no. 2017A010104004). H. Xu, T. Zhang and J. Arboil thank the funding from Generalitat de Catalunya 2017 SGR 327 and the Spanish MINECO ENE2017-85087-C3. ICN2 acknowledges support from the Severo Ochoa Programme (MINECO, Grant no. SEV-2013-0295) and is funded by the CERCA Programme / Generalitat de Catalunya. J. Llorca is a Serra Hùnter Fellow and is grateful to ICREA Academia program and to MINECO/FEDER grant ENE2015-63969-R and funding from Generalitat de Catalunya 2017 SGR 128. H. Xu and T. Zhang thank the CSC-UAB PhD scholarship program. Part of the present work has been performed in the framework of Universitat Autònoma de Barcelona Materials Science PhD program.

## ABBREVIATIONS

NPs nanoparticles  
LIBs lithium-ion batteries  
SIBs sodium-ion batteries  
KIBs potassium-ion bat-teries  
CB carbon black  
OAm, oleylamine  
OAc oleic acid  
TOP tri-*n*-octylphosphine  
PVDF polyvinylidene fluoride  
NMP N-methyl-2-pyrrolidone  
EC ethylene carbonate  
DEC diethyl car-bonate  
FEC fluoroethylene carbonate  
KTFSI potassium bis-trifluoromethanesulfonylimide  
DME diglyme  
XRD X-ray power diffraction  
SEM scanning electron microscopy  
TEM transmission electron microscopy  
STEM scanning TEM  
HRTEM high-resolution TEM  
HAADF High angle annular dark-field  
EELS electron energy loss spectroscopy  
EDS energy dispersive X-ray spectroscopy  
XPS X-ray photoelectron spectroscopy  
FTIR Fourier transform infrared spectrometer  
BET Brunauer–Emmet–Teller  
BJH Barrett–Joyner–Halenda  
CV cyclic voltammetry  
EIS Electrochemical impedance spectroscopy  
SEI solid-electrolyte interface

## REFERENCES

- (1) Palacín, M. R. Recent Advances in Rechargeable Battery Materials: A Chemist's Perspective. *Chem. Soc. Rev.* **2009**, 38 (9), 2565–2575.
- (2) Nitta, N.; Wu, F.; Lee, J. T.; Yushin, G. Li-Ion Battery Materials: Present and Future. *Mater. Today* **2015**, 18 (5), 252–264.
- (3) Obrovac, M. N.; Chevrie, V. L. Alloy Negative Electrodes for Li-Ion Batteries. *Chem. Rev.* **2014**, 114 (23), 11444–11502.



- (4) Marom, R.; Amalraj, S. F.; Leifer, N.; Jacob, D.; Aurbach, D. A Review of Advanced and Practical Lithium Battery Materials. *J. Mater. Chem.* **2011**, *21* (27), 9938–9954.
- (5) Tian, H.; Xin, F.; Wang, X.; He, W.; Han, W. High Capacity Group-IV Elements (Si, Ge, Sn) Based Anodes for Lithium-Ion Batteries. *J. Mater.* **2015**, *1* (3), 153–169.
- (6) Li, W.; Sun, X.; Yu, Y. Si-, Ge-, Sn-Based Anode Materials for Lithium-Ion Batteries: From Structure Design to Electrochemical Performance. *Small Methods* **2017**, *1* (3), 1600037.
- (7) Liu, J.; Song, K.; Zhu, C.; Chen, C. C.; Van Aken, P. A.; Maier, J.; Yu, Y. Ge/C Nanowires as High-Capacity and Long-Life Anode Materials for Li-Ion Batteries. *ACS Nano* **2014**, *8* (7), 7051–7059.
- (8) Zhang, H.; Huang, X.; Noonan, O.; Zhou, L.; Yu, C. Tailored Yolk–Shell Sn@C Nanoboxes for High-Performance Lithium Storage. *Adv. Funct. Mater.* **2017**, *27* (8), 1606023.
- (9) Wu, C.; Maier, J.; Yu, Y. Sn-Based Nanoparticles Encapsulated in a Porous 3D Graphene Network: Advanced Anodes for High-Rate and Long Life Li-Ion Batteries. *Adv. Funct. Mater.* **2015**, *25* (23), 3488–3496.
- (10) Liu, J.; Yu, L.; Wu, C.; Wen, Y.; Yin, K.; Chiang, F. K.; Hu, R.; Liu, J.; Sun, L.; Gu, L.; Maier, J.; Yu, Y.; Zhu, M. New Nanoconfined Galvanic Replacement Synthesis of Hollow Sb@C Yolk-Shell Spheres Constituting a Stable Anode for High-Rate Li/Na-Ion Batteries. *Nano Lett.* **2017**, *17* (3), 2034–2042.
- (11) Mauger, A.; Julien, C. M. Critical Review on Lithium-Ion Batteries: Are They Safe? Sustainable? *Ionics (Kiel)*. **2017**, *23* (8), 1933–1947.
- (12) Wen, J.; Yu, Y.; Chen, C. A Review on Lithium-Ion Batteries Safety Issues: Existing Problems and Possible Solutions. *Mater. Express* **2012**, *2* (3), 197–212.
- (13) Huang, X.; Cui, S.; Chang, J.; Hallac, P. B.; Fell, C. R.; Luo, Y.; Metz, B.; Jiang, J.; Hurley, P. T.; Chen, J. A Hierarchical Tin/Carbon Composite as an Anode for Lithium-Ion Batteries with a Long Cycle Life. *Angew. Chemie - Int. Ed.* **2015**, *54* (5), 1490–1493.
- (14) Zhang, Y.; Jiang, L.; Wang, C. Preparation of a Porous Sn@C Nanocomposite as a High-Performance Anode Material for Lithium-Ion Batteries. *Nanoscale* **2015**, *7* (28), 11940–11944.
- (15) Kamali, A. R.; Fray, D. J. Tin-Based Materials as Advanced Anode Materials for Lithium Ion Batteries: A Review. *Rev. Adv. Mater. Sci.* **2011**, *27* (1), 14–24.
- (16) Cho, H. H.; Glazer, M. P. B.; Dunand, D. C. Modeling of Stresses and Strains during (De)Lithiation of Ni<sub>3</sub>Sn<sub>2</sub>-Coated Nickel Inverse-Opal Anodes. *ACS Appl. Mater. Interfaces* **2017**, *9* (18), 15433–15438.
- (17) Wang, Z.; Wang, D.; Luo, S.; Bao, S.; Liu, Y.; Qi, X.; He, C.; Shi, C.; Zhao, N. Three-Dimensional Porous Bowl-Shaped Carbon Cages Interspersed with Carbon Coated Ni-Sn Alloy Nanoparticles as Anode Materials for High-Performance Lithium-Ion Batteries. *New J. Chem.* **2016**, *41* (1), 393–402.
- (18) Li, X.; He, X.; Xu, Y.; Huang, L.; Li, J.; Sun, S.; Zhao, J. Superiority of the Bi-Phasic Mixture of a Tin-Based Alloy Nanocomposite as the Anode for Lithium Ion Batteries. *J. Mater. Chem. A* **2015**, *3* (7), 3794–3800.
- (19) Park, M. G.; Lee, D. H.; Jung, H.; Choi, J. H.; Park, C. M. Sn-Based Nanocomposite for Li-Ion Battery Anode with High Energy Density, Rate Capability, and Reversibility. *ACS Nano* **2018**, *12* (3), 2955–2967.
- (20) Mahmood, N.; Zhu, J.; Rehman, S.; Li, Q.; Hou, Y. Control over Large-Volume Changes of Lithium Battery Anodes via Active-Inactive Metal Alloy Embedded in Porous Carbon. *Nano Energy* **2015**, *15*, 755–765.
- (21) Milanova, V. L.; Piskin, M. B.; Petrov, T. I.; Stankulov, T. E.; Denev, I. D.; Markova, I. N. Ni-Sn Alloy Carbon-Containing Nanocomposites as Alternative Anode Materials to the Graphite Electrodes in Li-Ion Batteries. *Rev. Adv. Mater. Sci* **2015**, *41*, 52–60.
- (22) Nguyen, T. L.; Kim, D. S.; Hur, J.; Park, M. S.; Kim, I. T. Ni-Sn-Based Hybrid Composite Anodes for High-Performance Lithium-Ion Batteries. *Electrochim. Acta* **2018**, *278*, 25–32.
- (23) Qin, J.; Zhang, X.; Zhao, N.; Shi, C.; Liu, E.; Li, J.; He, C. Carbon-Coated Ni<sub>3</sub>Sn<sub>2</sub> Nanoparticles Embedded in Porous Carbon Nanosheets as a Lithium Ion Battery Anode with Outstanding Cycling Stability. *RSC Adv.* **2014**, *4* (90), 49247–49256.
- (24) Ying, H.; Han, W. Q. Metallic Sn-Based Anode Materials: Application in High-Performance Lithium-Ion and Sodium-Ion Batteries. *Adv. Sci.* **2017**, *4* (11), 1700298.
- (25) Shi, X.; Song, H.; Li, A.; Chen, X.; Zhou, J.; Ma, Z. Sn-Co Nanoalloys Embedded in Porous N-Doped Carbon Microboxes as a Stable Anode Material for Lithium-Ion Batteries. *J. Mater. Chem. A* **2017**, *5* (12), 5873–5879.

- (26) Xu, Y. S.; Duan, S. Y.; Sun, Y. G.; Bin, D. S.; Tao, X. Sen; Zhang, D.; Liu, Y.; Cao, A. M.; Wan, L. J. Recent Developments in Electrode Materials for Potassium-Ion Batteries. *J. Mater. Chem. A* **2019**, 7 (9), 4334–4352.
- (27) Vaalma, C.; Buchholz, D.; Weil, M.; Passerini, S. A Cost and Resource Analysis of Sodium-Ion Batteries. *Nat. Rev. Mater.* **2018**, 3 (4), 18013.
- (28) Huang, K.; Xing, Z.; Wang, L.; Wu, X.; Zhao, W.; Qi, X.; Wang, H.; Ju, Z. Direct Synthesis of 3D Hierarchically Porous Carbon/Sn Composites via in Situ Generated NaCl Crystals as Templates for Potassium-Ion Batteries Anode. *J. Mater. Chem. A* **2018**, 6 (2), 434–442.
- (29) Li, J.; Xu, X.; Luo, Z.; Zhang, C.; Yu, X.; Zuo, Y.; Zhang, T.; Tang, P.; Arbiol, J.; Llorca, J.; Liu, J.; Cabot, A. Compositionally Tuned Ni<sub>x</sub>Sn Alloys as Anode Materials for Lithium-Ion and Sodium-Ion Batteries with a High Pseudocapacitive Contribution. *Electrochim. Acta* **2019**, 304, 246–254.
- (30) Li, J.; Xu, X.; Luo, Z.; Zhang, C.; Zuo, Y.; Zhang, T.; Tang, P.; Infante-Carrió, M. F.; Arbiol, J.; Llorca, J.; Liu, J.; Cabot, A. Co–Sn Nanocrystalline Solid Solutions as Anode Materials in Lithium-Ion Batteries with High Pseudocapacitive Contribution. *ChemSusChem* **2019**, 12 (7), 1451–1458.
- (31) Liu, J.; Wang, S.; Kravchyk, K.; Ibáñez, M.; Krumeich, F.; Widmer, R.; Nasios, D.; Meyns, M.; Llorca, J.; Arbiol, J.; Kovalenko, M. V.; Cabot, A. SnP Nanocrystals as Anode Materials for Na-Ion Batteries. *J. Mater. Chem. A* **2018**, 6 (23), 10958–10966.
- (32) He, M.; Walter, M.; Kravchyk, K. V.; Erni, R.; Widmer, R.; Kovalenko, M. V. Monodisperse SnSb Nanocrystals for Li-Ion and Na-Ion Battery Anodes: Synergy and Dissonance between Sn and Sb. *Nanoscale* **2015**, 7 (2), 455–459.
- (33) Liu, J.; Kopold, P.; Wu, C.; Van Aken, P. A.; Maier, J.; Yu, Y. Uniform Yolk-Shell Sn<sub>4</sub>P<sub>3</sub>@C Nanospheres as High-Capacity and Cycle-Stable Anode Materials for Sodium-Ion Batteries. *Energy Environ. Sci.* **2015**, 8 (12), 3531–3538.
- (34) Fjellvåg, H.; Kjekshus, A.; Stomberg, R.; Zingales, R.; Vikholm, I.; Urso, F.; Weidlein, J.; Zingaro, R. A. Structural Properties of Co<sub>3</sub>Sn<sub>2</sub>, Ni<sub>3</sub>Sn<sub>2</sub> and Some Ternary Derivatives. *Acta Chem. Scand.* **1986**, 40a, 23–30.
- (35) Li, J.; Luo, Z.; Zuo, Y.; Liu, J.; Zhang, T.; Tang, P.; Arbiol, J.; Llorca, J.; Cabot, A. NiSn Bimetallic Nanoparticles as Stable Electrocatalysts for Methanol Oxidation Reaction. *Appl. Catal. B Environ.* **2018**, 234, 10–18.
- (36) He, M.; Protesescu, L.; Caputo, R.; Krumeich, F.; Kovalenko, M. V. A General Synthesis Strategy for Monodisperse Metallic and Metalloid Nanoparticles (In, Ga, Bi, Sb, Zn, Cu, Sn, and Their Alloys) via in Situ Formed Metal Long-Chain Amides. *Chem. Mater.* **2015**, 27 (2), 635–647.
- (37) Li, J.; Luo, Z.; He, F.; Zuo, Y.; Zhang, C.; Liu, J.; Yu, X.; Du, R.; Zhang, T.; Infante-Carrió, M. F.; Tang, P.; Arbiol, J.; Llorca, J.; Cabot, A. Colloidal Ni-Co-Sn Nanoparticles as Efficient Electrocatalysts for the Methanol Oxidation Reaction. *J. Mater. Chem. A* **2018**, 6 (45), 22915–22924.
- (38) Li, J.; Zuo, Y.; Liu, J.; Wang, X.; Yu, X.; Du, R.; Zhang, T.; Infante-Carrió, M. F.; Tang, P.; Arbiol, J.; Llorca, J.; Luo, Z.; Cabot, A. Superior Methanol Electrooxidation Performance of (110)-Faceted Nickel Polyhedral Nanocrystals. *J. Mater. Chem. A* **2019**, 7 (38), 22036–22043.
- (39) Nafria, R.; Genç, A.; Ibáñez, M.; Arbiol, J.; Ramírez De La Piscina, P.; Homs, N.; Cabot, A. Co-Cu Nanoparticles: Synthesis by Galvanic Replacement and Phase Rearrangement during Catalytic Activation. *Langmuir* **2016**, 32 (9), 2267–2276.
- (40) Vogt, L. O.; Villevieille, C. Elucidation of the Reaction Mechanisms of Isostructural FeSn<sub>2</sub> and CoSn<sub>2</sub> Negative Electrodes for Na-Ion Batteries. *J. Mater. Chem. A* **2017**, 5 (8), 3865–3874.
- (41) Liu, J.; Wen, Y.; Van Aken, P. A.; Maier, J.; Yu, Y. Facile Synthesis of Highly Porous Ni-Sn Intermetallic Microcages with Excellent Electrochemical Performance for Lithium and Sodium Storage. *Nano Lett.* **2014**, 14 (11), 6387–6392.
- (42) Xin, F. X.; Tian, H. J.; Wang, X. L.; Xu, W.; Zheng, W. G.; Han, W. Q. Enhanced Electrochemical Performance of Fe<sub>0.74</sub>Sn<sub>5</sub>@Reduced Graphene Oxide Nanocomposite Anodes for Both Li-Ion and Na-Ion Batteries. *ACS Appl. Mater. Interfaces* **2015**, 7 (15), 7912–7919.
- (43) Wang, S.; He, M.; Walter, M.; Krumeich, F.; Kravchyk, K. V.; Kovalenko, M. V. Monodisperse CoSn<sub>2</sub> and FeSn<sub>2</sub> Nanocrystals as High-Performance Anode Materials for Lithium-Ion Batteries. *Nanoscale* **2018**, 10 (15), 6827–6831.

- (44) He, Y.; Li, A.; Dong, C.; Li, C.; Xu, L. Mesoporous Tin-Based Oxide Nanospheres/Reduced Graphene Composites as Advanced Anodes for Lithium-Ion Half/Full Cells and Sodium-Ion Batteries. *Chem. - A Eur. J.* **2017**, 23 (55), 13724–13733.
- (45) Qin, J.; Liu, D.; Zhang, X.; Zhao, N.; Shi, C.; Liu, E. Z.; He, F.; Ma, L.; Li, Q.; Li, J.; He, C. One-Step Synthesis of SnCo Nanoconfined in Hierarchical Carbon Nanostructures for Lithium Ion Battery Anode. *Nanoscale* **2017**, 9 (41), 15856–15864.
- (46) Yang, L.; Li, X.; He, S.; Du, G.; Yu, X.; Liu, J.; Gao, Q.; Hu, R.; Zhu, M. Mesoporous Mo<sub>2</sub>C/N-Doped Carbon Heteronanowires as High-Rate and Long-Life Anode Materials for Li-Ion Batteries. *J. Mater. Chem. A* **2016**, 4 (28), 10842–10849.
- (47) Yu, P.; Popov, B. N.; Ritter, J. A.; White, R. E. Determination of the Lithium Ion Diffusion Coefficient in Graphite. *J. Electrochem. Soc.* **1999**, 146 (1), 8–14.
- (48) Brezesinski, T.; Wang, J.; Tolbert, S. H.; Dunn, B. Ordered Mesoporous  $\alpha$ -MoO<sub>3</sub> with Iso-Oriented Nanocrystalline Walls for Thin-Film Pseudocapacitors. *Nat. Mater.* **2010**, 9 (2), 146–151.
- (49) Xu, X.; Liu, J.; Liu, J.; Ouyang, L.; Hu, R.; Wang, H.; Yang, L.; Zhu, M. A General Metal-Organic Framework (MOF)-Derived Selenidation Strategy for In Situ Carbon-Encapsulated Metal Selenides as High-Rate Anodes for Na-Ion Batteries. *Adv. Funct. Mater.* **2018**, 28 (16), 1707573.
- (50) Kim, H.-S.; Cook, J. B.; Tolbert, S. H.; Dunn, B. The Development of Pseudocapacitive Properties in Nanosized-MoO<sub>3</sub>. *J. Electrochem. Soc.* **2015**, 162 (5), A5083–A5090.
- (51) Zhang, C.; Biendicho, J. J.; Zhang, T.; Du, R.; Li, J.; Yang, X.; Arbiol, J.; Zhou, Y.; Morante, J. R.; Cabot, A. Combined High Catalytic Activity and Efficient Polar Tubular Nanostructure in Urchin-Like Metallic NiCo<sub>2</sub>Se<sub>4</sub> for High-Performance Lithium–Sulfur Batteries. *Adv. Funct. Mater.* **2019**, 29, 1903842.
- (52) Chen, C.; Wen, Y.; Hu, X.; Ji, X.; Yan, M.; Mai, L.; Hu, P.; Shan, B.; Huang, Y. Na<sup>+</sup> Intercalation Pseudocapacitance in Graphene-Coupled Titanium Oxide Enabling Ultra-Fast Sodium Storage and Long-Term Cycling. *Nat. Commun.* **2015**, 6 (1), 6929.
- (53) Zhang, K.; Park, M.; Zhou, L.; Lee, G.-H.; Shin, J.; Hu, Z.; Chou, S.-L.; Chen, J.; Kang, Y.-M. Cobalt-Doped FeS<sub>2</sub> Nanospheres with Complete Solid Solubility as a High-Performance Anode Material for Sodium-Ion Batteries. *Angew. Chemie Int. Ed.* **2016**, 55 (41), 12822–12826.
- (54) Jiang, Y.; Liu, J. Definitions of Pseudocapacitive Materials: A Brief Review. *Energy Environ. Mater.* **2019**, 2 (1), 30–37.
- (55) Augustyn, V.; Simon, P.; Dunn, B. Pseudocapacitive Oxide Materials for High-Rate Electrochemical Energy Storage. *Energy Environ. Sci.* **2014**, 7 (5), 1597–1614.
- (56) Sultana, I.; Rahman, M. M.; Chen, Y.; Glushenkov, A. M. Potassium-Ion Battery Anode Materials Operating through the Alloying–Dealloying Reaction Mechanism. *Adv. Funct. Mater.* **2018**, 28 (5), 1703857.

Graphical Abstract

